Check for updates

Characterization of integrated waveguides by atomic-force-microscopy-assisted mid-infrared imaging and spectroscopy

KEVIN GALLACHER,[1] ROSS W. MILLAR,[1] DOUGLAS J. PAUL,[1] JACOPO FRIGERIO,[2] ANDREA BALLABIO,[2] GIOVANNI ISELLA,[2] FRANCESCO RUSCONI,[3] PAOLO BIAGIONI,[3] VALERIA GILIBERTI,[4] ALESSIA SORGI,[5,6] LEONETTA BALDASSARRE,[7] AND MICHELE ORTOLANI[4,7,*]

[1]*University of Glasgow, James Watt School of Engineering, Rankine Building, Oakfield Avenue, Glasgow G12 8LT, UK*
[2]*L-NESS, Dipartimento di Fisica, Politecnico di Milano, Via Anzani 42, I-22100 Como, Italy*
[3]*Dipartimento di Fisica, Politecnico di Milano, Piazza Leonardo Da Vinci 32, I-20133 Milan, Italy*
[4]*Istituto Italiano di Tecnologia, Center for Life Nanoscience, Viale Regina Elena 291, I-00161 Rome, Italy*
[5]*Istituto Nazionale di Ottica INO-CNR, Largo E. Fermi 6, I-50125 Florence, Italy*
[6]*LENS, European Laboratory for Nonlinear Spectroscopy, Via N. Carrara 1, I-50019 Sesto Fiorentino, Italy*
[7]*Dipartimento di Fisica, Universitá di Roma La Sapienza, Piazzale Aldo Moro 5, I-00185 Rome, Italy*
*michele.ortolani@roma1.infn.it

Abstract: A novel spectroscopy technique to enable the rapid characterization of discrete mid-infrared integrated photonic waveguides is demonstrated. The technique utilizes lithography patterned polymer blocks that absorb light strongly within the molecular fingerprint region. These act as integrated waveguide detectors when combined with an atomic force microscope that measures the photothermal expansion when infrared light is guided to the block. As a proof of concept, the technique is used to experimentally characterize propagation loss and grating coupler response of Ge-on-Si waveguides at wavelengths from 6 to 10 μm. In addition, when the microscope is operated in scanning mode at fixed wavelength, the guided mode exiting the output facet is imaged with a lateral resolution better than 500 nm i.e. below the diffraction limit. The characterization technique can be applied to any mid-infrared waveguide platform and can provide non-destructive in-situ testing of discrete waveguide components.

1. Introduction

Mid-infrared (MIR) photonic integrated circuits (PICs) [1,2] are receiving considerable attention due to the variety of envisaged applications in security [3], medical diagnostics [4,5], biochemistry studies [6] and environmental monitoring [7,8]. This is primarily because chemical compounds can be identified with high specificity by interrogating unique vibrational modes, which absorb light within the molecular 'fingerprint' region (wavelength λ between 5 and 20 μm) [9]. Several MIR waveguide platforms have been demonstrated in this range including chalcogenides [10], HgCdTe [11], GaAs [12], SiGe [13,14], and Ge-on-Si [15–17]. To enable low-cost approaches based on silicon foundry compatible materials such as Ge and SiGe are to be preferred, since production could take advantage of existing silicon photonics infrastructure [18]. The realization of a MIR PIC for molecular absorption spectroscopy requires a broad suite of components including sources [19], non-linear conversion [20,21], detectors [22,23], micro-fluidics [24],

waveguide sensors [25,26], plasmonic field enhancement [27,28], polarization control [29], resonators [30], gratings [31,32], and interferometers [33,34].

The characterization of the PIC components for the MIR with standard optical-fiber-coupling techniques can be challenging due to the lack of efficient MIR-transparent optical fiber. As an alternative to fiber-optic techniques, free-space end-fire coupling setups are employed, which can be difficult to align because of the large blackbody radiation background in the MIR. Techniques enabling an on-chip measurements of the components, without the requirement of an external detector, would allow a faster and more reliable characterization method. Near-field optical microscopy performed with scanning atomic force microscopy (AFM) probes is one such technique that has been proposed for on-chip characterization [35–38]. In this work we apply to waveguide characterization, to our knowledge for the first time, photothermal expansion measurements with infrared light and contact-mode AFM probes (the so-called AFM-IR technique or photothermal-induced resonance technique (PTIR) [39–41]). We demonstrate an integrated waveguide detector utilizing a lithography patternable polymer that strongly absorbs in the molecular 'fingerprint' region (SU8) and use an AFM probe to measure the photothermal expansion of the polymer when exposed to light guided from the waveguide (see Fig. 1).
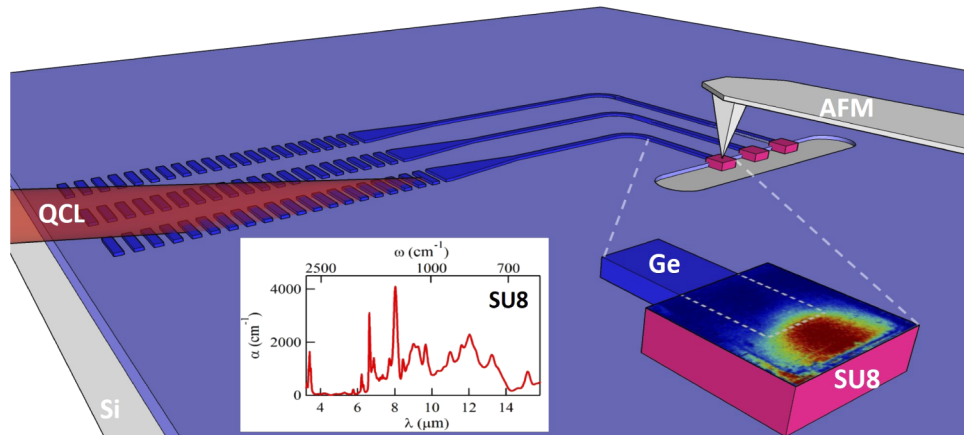
Fig. 1. (a) A schematic diagram of the proposed atomic force microscopy coupled to infrared spectroscopy technique (AFM-IR) for characterization of photonic integrated waveguide circuits operating within the molecular 'fingerprint' region ($\lambda = 5 - 20\mu m$). An external quantum cascade laser (QCL) is coupled to the waveguide (Ge-on-Si) by a grating coupler before light is directed to a patterned polymer block (SU8), which absorbs the light and the photothermal response can then be measured by the AFM probe. Inset: the absorption spectrum of SU8 measured by FTIR spectroscopy.

The AFM-IR technique provides flexibility since the polymer can be patterned at any point on a waveguide and employing a polymer that is removable enables non-destructive testing that could be used at different stages of device fabrication or PIC optimisation. For example this could be useful for characterization of individual components of a complex PIC, to measure in-situ insertion losses of components before or after the heterogeneous integration of sources such as quantum cascade lasers (QCL). This technique also enables sub-diffraction imaging of the near-field patterns, which could be used to image the output of a multi-mode waveguide or interference device when the AFM is operated in scanning mode. Visualization of near-field patterns by AFM-IR exploiting polymer coating of the device under test has been previously reported for the case of plasmonic nanoantennas [42–45]. To demonstrate the AFM-IR technique for waveguide characterization, the propagation loss and grating coupler response of Ge-on-Si

waveguides is measured from $\lambda = 6$ to $10\,\mu$m. Near-field imaging of a single-mode Ge-on-Si waveguide with a lateral resolution better than 500 nm is also demonstrated.

2. AFM-IR waveguide characterization technique

Existing far-field characterization methods for waveguide chips, based on the observation with a MIR camera of radiation emitted from the chip surface [16] or side facet, can provide a full picture of millimeter-scale chips, however their lateral resolution is limited by diffraction in free-space, which, in the MIR, results in an imaging resolution of several tens of μm. Moreover, they cannot access evanescent fields. Scattering scanning near-field optical microscopy (SNOM), performed with scanning AFM probes illuminated with an external laser beam, has been previously proposed for waveguide chip characterization [35–38]. Therein, the local modal field scattered by the probe tip operated in tapping mode is probed for each position of the tip itself. Beyond the scattering function probed by SNOM, the absorption of MIR radiation emitted by pulsed laser beams in sub-wavelength structures can also be locally measured with an AFM probe in a mechanical fashion, by detecting the local photothermal expansion of the transiently heated portion of the sample. This technique, initially proposed by Dazzi et al. with the name of PTIR [39] and then named AFM-IR, exploits mechanical resonances of the AFM cantilever in the millisecond time scale to increase sensitivity to sub-nanometer expansions at controlled times triggered by the laser pulses. AFM-IR has been widely employed to obtain information related to MIR absorption at the sub-wavelength scale [39–41,45–49], both in the form of absorption maps and spectra.

In this work we exploit AFM-IR with contact-mode AFM probes for waveguide chip characterization for the first time. AFM-IR is used to image the local intensity pattern in MIR-absorbing polymer blocks lithographically patterned at the PIC test locations, e.g. a waveguide output facet. The many vibrational peaks of the polymer continuously cover a nonzero absorption range in the MIR of $\lambda \approx 6 - 14\,\mu$m. In conjunction with the wavelength-independent sensitivity of the AFM probe tip, the SU8 blocks act as an on-chip-integrated spectral intensity detectors. We demonstrate that the novel technique can be used to measure waveguide propagation losses and to spectrally characterize complex PIC structures such as Bragg grating couplers (Fig. 1).

In general the lateral imaging resolution of AFM-IR is limited by the thermal diffusion lengths and by the thermal conduction in the sample, which may lead to homogeneous heating of volumes larger than the sub-wavelength MIR absorption volume. To increase the lateral resolution and obtain sub-diffraction imaging, the MIR absorber should preferably be a good thermal insulator. In this case, the temperature increase map almost corresponds to the heat source map, and therefore to the field intensity map. In this work we employ the polymer SU8, which features strong MIR absorption fingerprints and low thermal conductivity of ~ 0.2 W/mK. SU8 blocks of $5 \times 5 \times 2\,\mu$m^3 are positioned on chip by lithography at the output facets of the waveguides (see Fig. 2(e)). AFM-IR has been brought to its extreme time resolution limits of nanoseconds by engineering nanophotonic probes for fast mechanical detection [50], and to its extreme lateral resolution limits of a few tens of nanometers exploiting MIR plasmonic field confinement by gold-coated probe tips [40,41]. Here we employed standard uncoated silicon cantilever probes, in order not to perturb the near-field intensity under investigation [44].

We have modified a commercial AFM-IR setup (Anasys Instruments NanoIR2) so as to focus the QCL beam at the waveguide input and to keep the AFM probe tip at the waveguide output. Note that in the original setup the position of the QCL focus and the position of the AFM probe tip coincide. In this way, only the radiation which has effectively traveled through the waveguide can be absorbed in the SU8 block. This spatial de-coupling is achieved by slightly changing the input angle of the collimated beam emitted by the QCL onto the focusing parabolic mirror included in the AFM-IR setup, which focuses the laser beam on the chip surface to a diffraction-limited spot size. The angle between the paraboloid axis and the chip surface normal has been kept at the original setup value of 70° so as to allow for immediate referencing of the output photo-expansion
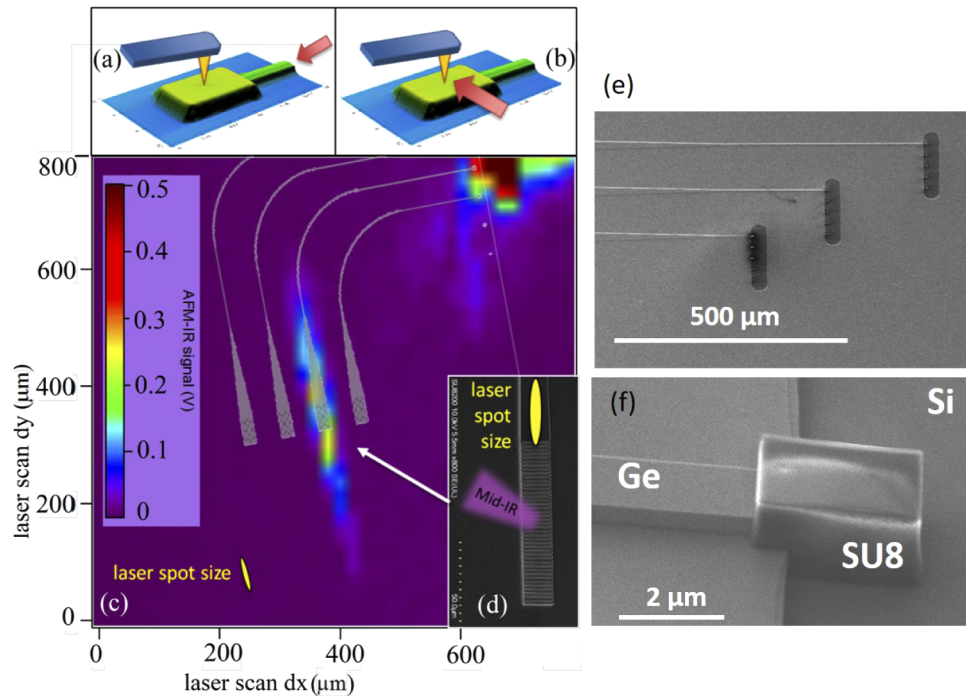
Fig. 2. (a,b) An AFM topography 3D render of a polymer SU8 block patterned at a Ge-on-Si rib waveguide end facet with a schematic overlay of the AFM probe and the light coupling direction (arrow). (a) The MIR radiation arrives to the SU8 block through the waveguide. (b) The direct illumination of the SU8 block. (c) A raster-scan plot of the AFM-IR signal obtained by scanning the laser spot with the AFM probe at a fixed position on top of the SU8 block. A scanning electron microscope (SEM) image of the fabricated Bragg grating coupler (d), Ge-on-Si rib waveguides (e) and patterned polymer SU8 block (f).

spectrum to the input spectrum. This was measured by directly illuminating the SU8 block with the AFM probe on top of it (the AFM probe, the laser focus position and the sample stage all have independent movement actuators). The original AFM-IR setup operates in *p*-polarization (with the electric field vector at 70° to the chip surface normal), so, for coupling the QCL radiation to the broadband TE mode of the waveguides [17], we rotated the polarization to *s* (electric field parallel to the chip surface) at all λ with a custom reflective periscope.

Our AFM-IR system contains a broadband tunable QCL (MIRcat-xB by Daylight Solutions Inc.), with four laser chips emitting between 5 and 11 μm, which was utilized for the broadband characterization of MIR PICs. As an example for an incident laser power of 5 mW this would result in a temperature increase of a few K [45] and photothermal expansions of the order of 10^{-11} m, when assuming a thermal expansion coefficient of 6×10^{-5} K^{-1}. To be able to detect these small photo-expansion levels, the repetition rate of the QCL was finely tuned at the mechanical resonance of the AFM silicon cantilever (≈ 200 kHz) to realize a driven harmonic oscillator [39,40]. The linear relation between pulse energy (product of peak QCL power times pulse duration) and the driven harmonic oscillator amplitude (hereafter named AFM-IR signal) has been experimentally verified over two orders of magnitude, allowing for relative spectral efficiency calibration in the MIR. For each individual spectral measurement, the AFM-IR signal is normalized by the independently measured ω-dependent laser power.

The spatial separation of the QCL focus and the AFM probe for our system is demonstrated in Fig. 2. The focussed QCL spot is raster-scanned, while the AFM probe is at a fixed position on

top of the SU8 block. When the QCL is positioned on the third grating coupler, an AFM-IR signal is clearly seen for approximately 10 points in the raster-scan plot, along a 100 μm long line (yellow pixels with medium-strong signal in the center of Fig. 2(c)). There is no signal present when the QCL spot is moved to adjacent grating couplers for fixed AFM probe position, which demonstrates the high spatial selectivity. The only other time an AFM-IR signal is observed is when the QCL spot directly illuminates the SU8 block. The direct illumination of the block provides a reference spectrum proportional to the polymer absorption coefficient $\alpha_{SU8}(\omega)$ through a fairly frequency-independent instrument transfer constant C which includes the sample thermal properties, the mechanical properties of the AFM cantilever and the sample thermal expansion coefficient [51]. This reference spectrum has been cross-checked with the $\alpha_{SU8}(\omega)$ obtained from Fourier-transform IR (FTIR) transmission spectra taken on thin polymer films. From the laser-power-normalized AFM-IR spectrum measured on the SU8 block $S(\omega)$, the spectral efficiency function for the waveguide component $F(\omega)$ can then be determined by inverting the following relation:

$$S(\omega) = C \cdot \alpha_{SU8}(\omega) \cdot F(\omega) \quad (1)$$

In principle $F(\omega)$ can be directly computed from $S(\omega)$ in a model-free fashion. If a model function is instead chosen for $F(\omega)$, e.g. a Gaussian peak function as we use here, then one can perform a fitting of Eq. (1) to the $S(\omega)$ data using $\alpha_{SU8}(\omega)$ as a tabulated vector and the numerical parameters of $F(\omega)$ (e.g. width σ, center frequency ω_0, intensity S_0) as fitting parameters:

$$S(\omega) = C \cdot \alpha_{SU8}(\omega) \cdot S_0 \exp^{-\left(\frac{(\omega_0-\omega)^2}{2\sigma^2}\right)}. \quad (2)$$

Clearly, the use of the optimal AFM-IR angle of incidence of 70° for grating couplers allows for immediate referencing of the measured $S(\omega)$ with the AFM probe at the end of the waveguide with those measured with the AFM probe on the SU8 block. Ideally, the AFM-IR signal measured on the block corresponds to $F = 1$ in Eq. (1), but actually it provides a system transfer function $F_0(\omega)$ that can be used for absolute calibration. Importantly, this procedure removes the need for fabricating and measuring a second reference waveguide on the same chip to characterize the waveguide under test, which is typical in far-field, fiber-optics and free-space waveguide characterization methods.
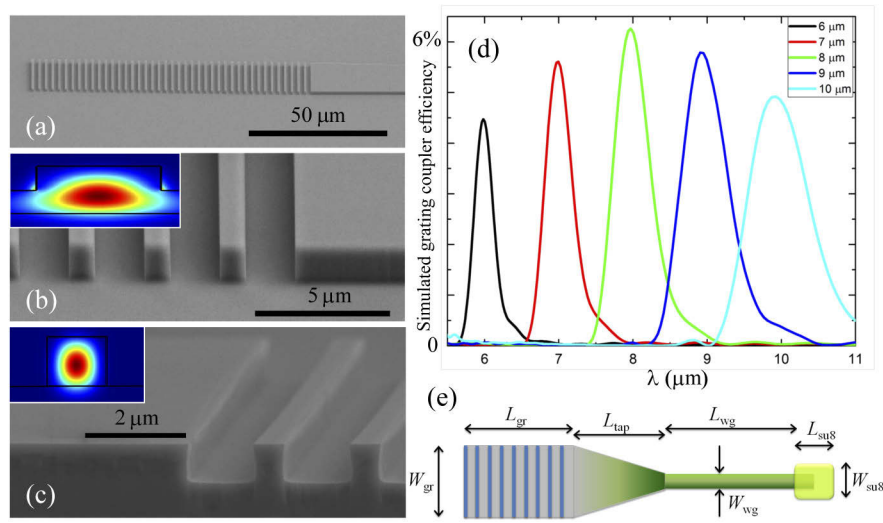
2.1. Ge-on-Si waveguide fabrication

A Ge epitaxial layer of 2 μm thickness was grown by low-energy plasma-enhanced chemical vapor deposition on a high resistivity Si (001) wafer [52]. Subsequently, 3.5 μm wide Ge-on-Si rib waveguides and Bragg grating couplers were fabricated by patterning HSQ with electron-beam lithography. A 3.5 μm wide Ge-on-Si rib waveguide provides single-mode operation over the full measurement range ($\lambda = 6 - 10$ μm). The grating coupler and rib waveguides were dry etched at the same time using a mixed gas process (SF$_6$ / C$_4$F$_8$) to a depth of approximately 1 μm. The lithography and etch processes have been optimized to produce highly anisotropic and ultra-smooth waveguide sidewalls [17]. Next, the remaining 1 μm thick Ge slab at the waveguide output was etched. This isolation etch ensures high coupling ($\sim$ 60%) from the rib waveguide into the SU8 block at the output facet. Lastly, the SU8 polymer blocks were patterned by electron-beam lithography and after development cured at 180°C.

2.2. Bragg grating couplers

The broadband sensitivity of the present technique can be exploited to measure on-chip the spectral properties of complex integrated photonic components, such as the Bragg grating couplers used in this work. Uniform Bragg gratings for TE polarization injection were designed at center wavelengths ranging between 6 and 10 μm (1 μm increments) using 2D finite-difference

time-domain (FDTD) simulations (FDTD Solutions, Lumerical Inc., Canada). The grating width (W_{gr}) and length (L_{gr}) were designed as 30 and 100 μm, respectively. This was to match the focussed QCL spot size of the AFM-IR system. Adiabatic linear tapers were designed for efficient power coupling between the multi-mode grating section and the single-mode waveguides. The pitch and duty cycle parameters of the gratings were calculated by using an optimization algorithm applied to 2D FDTD results [53]. The simulated coupling efficiency spectra for the gratings are shown in Fig. 3(d). The bandwidth of the gratings is in the range of 0.1 - 0.4 μm and the coupling efficiency is 6%, which is in-line with previously demonstrated Ge-on-Si uniform Bragg gratings that are injected with a TE polarization [32]. The fabricated gratings were characterized by scanning the QCL emission wavelength, while the AFM probe was positioned on the corresponding SU8 block. The measured AFM-IR spectrum for each grating is shown in Fig. 4.


Fig. 3. (a) A SEM image of a fabricated Ge-on-Si grating coupler. (b, c) SEM detailed views of the etched grating walls in the different rib (b) and ridge (c) waveguide platforms. (d) The modelled coupling efficiency as a function of λ for the grating couplers designed with center wavelengths of 6, 7, 8, 9, and 10 μm. (e) A schematic diagram of the Bragg grating coupler with linear inverse taper, and single-mode waveguide section with a patterned polymer absorber block.

Table 1. Comparison of simulated and experimental Ge-on-Si Bragg grating couplers.

λ_{design} (μm)	ω_{design} (cm^{-1})	ω_{exp} (cm^{-1})	σ_{design} (cm^{-1})	σ_{exp} (cm^{-1})	Period (μm)	Duty cycle (%)
6.0	1666	1702	34	25	2.050	66.2
6.6	1510	1545	37	30	2.466	64.9
7.0	1428	1461	39	32	2.612	65.6
8.0	1250	1286	41	34	3.017	65.3
9.0	1111	1162	42	35	3.407	66.8
10.0	1000	1041	43	35	3.806	65.9

The data fitting procedure described in Eq. (2) was employed to extract the experimental values for the center frequency ω_{exp} and width σ_{exp} of the grating coupling efficiency spectrum
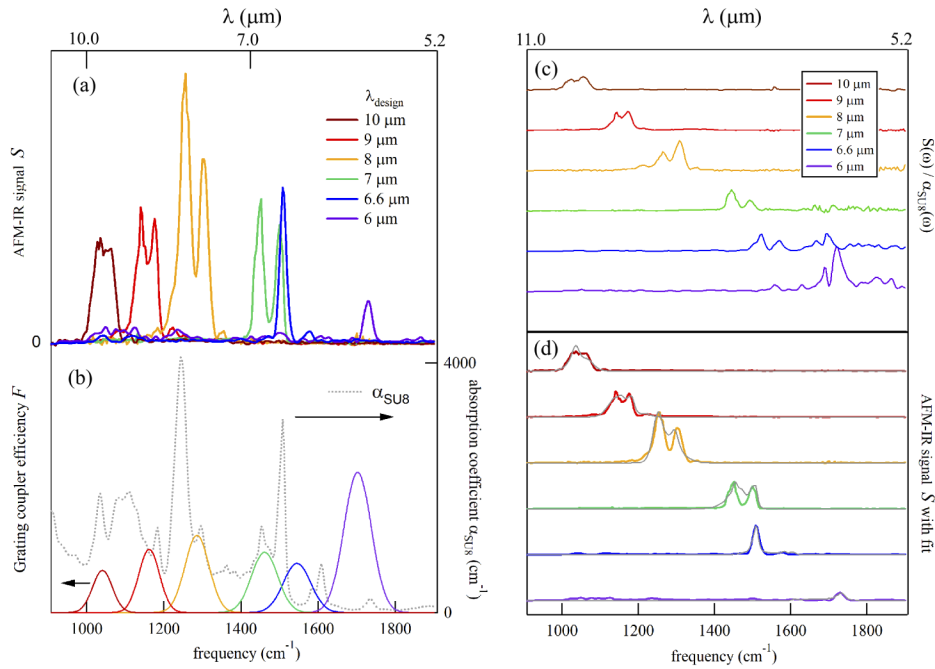
Fig. 4. The AFM-IR spectra measured at the end of the waveguides with different grating couplers. (a) The raw AFM-IR spectra for six waveguides and (b) the color-code-corresponding Gaussian model of the spectral coupling efficiency based on Eq. (2). The SU8 absorption coefficient is also reported as a grey dotted line. (c) The result of the division of the raw data in (a) by α_{SU8} in (b). (d) The fitting curves based on Eq. (2) (grey) superimposed to the raw data shown in (a). The discrepancy in the linewidths is related to numerical artifacts of the interpolation of the FTIR data on the wavenumber axis of the AFM-IR data. From the standard deviation of the extracted parameters from several identical samples, we estimate a precision of ± 5% for the center wavelengths and widths reported in Table 1, and ± 50% for the coupling efficiency (not reported in Table 1).

$F(\omega)$ as defined in Eq. (1). In this case, no major difference was observed between the α_{SU8} measured by FTIR transmission spectroscopy on a thick film and the reference spectrum taken with the AFM probe on top of the SU8 block, therefore the FTIR data were directly employed in Eq. (2) due to their higher signal-to-noise ratio. The design Gaussian width σ_{design} was obtained by fitting the results of FDTD simulations in Fig. 3(d) and by converting them in frequency units instead of wavelength units. In Table 1 it can be observed that a good match between design and experimental frequencies is obtained across the measurement range of 6 to 10 μm. The experimental bandwidths are slightly lower than the simulated ones. A small discrepancy is expected since the 2D FDTD simulations were performed with an injected Gaussian beam, rather than the elliptical spot size provided by the AFM-IR system. This elliptical spot size is likely to be the reason why a low efficiency spectrum in the range 1-2% was observed, against a simulated efficiency of 5-10% in Fig. 3. The narrow spectral coupling efficiency peaks observed in Fig. 4(b), (c) and (d), positioned at different wavelengths according to the different grating designs, demonstrate the excellent wavelength selectivity of the grating couplers.

2.3. Propagation loss

The propagation loss of the Ge-on-Si rib waveguides have been measured by the AFM-IR technique by observing spectral intensity oscillations (fringes) due to a Fabry-Perot cavity that

forms between the waveguide output facet and the grating coupler. The cavity length is equal to the sum of the taper length (L_{tap}) plus the single-mode waveguide section L_{wg} (see Fig. 3(e)). From 2D FDTD modelling a 20% reflection at the interface between the waveguide output facet and the SU8 polymer block, and a 5% reflection from the grating coupler is calculated. For the cavity lengths under investigation, the expected fringe period ranges from 2 to 5 cm^{-1} when assuming the bulk refractive index of Ge. The linewidth of the QCL in non-stabilized pulsed mode is ≈ 1 cm^{-1}, so the frequency-scan resolution was set to 1.0 cm^{-1}, which is sufficient to observe the fringes.

The experimental measured fringes are shown in Fig. 5 for the three waveguide cavity lengths that were measured (250, 350, 400 μm). In the inset of Fig. 5(a), a linear fit to the measured fringe period as a function of cavity length is shown, which gives a modal index of 3.7 ± 0.1 at $\lambda = 5.8$ μm, and this is in good agreement with the finite difference eigenmode simulations. The propagation loss can be obtained through the formula [54]:

$$\alpha(\frac{dB}{cm}) = -\frac{4.34}{L_{tap} + L_{wg}} \ln\left(\frac{1 - \sqrt{1 - K^2}}{K\sqrt{R_1 R_2}}\right) \tag{3}$$

$$K = \frac{I_{max} - I_{min}}{I_{max} + I_{min}}, \tag{4}$$

where R_1 is the reflectivity at the grating/taper interface, R_2 is the reflectivity at the waveguide output facet, 4.34 is the conversion factor to dB/cm, and I_{max} and I_{min} are the maximum and minimum fringe intensities, respectively evaluated with a fit of a sinusoidal function to the data in Fig. 5. Only two fringes were used at the center of the oscillating spectral pattern, so as to approximate SU8 absorption and grating coupling efficiency to two constant values that are removed in the definition of K in Eq. (4). The calculation provides propagation loss values of 3 ± 2 dB/cm at $\lambda = 6$ μm, where the large uncertainty is dominated by the relatively high value of the frequency-scan resolution of 1.0 cm^{-1} if compared to fringe periods of $3 - 5$ cm^{-1} (see Table 2), which produces undersampling of the fringes.

**Table 2. The calculated and experimental Fabry-Perot fringe periods.**

Length (μm)	$\Delta\omega_{calc}$	$\Delta\omega_{exp}$
250	5.0	4.6
350	3.6	3.3
400	2.8	3.0

The typical uncertainty obtained in standard end-fire coupling setups due to alignment of an external detector is usually at least 1 dB, so it becomes relevant for our low-loss waveguides. Our AFM-IR setup bypasses the end-fire out-coupling problem, as the detection takes place on the chip surface. An alternative method to Fabry-Perot fringe contrast evaluation is the quasi cut-back method, in which waveguides of different length are realized on the same chip and the output power is measured by displacing the chip. Presently, the measurement of different waveguides realized on the same chip requires improvement of the AFM-IR beam-steering apparatus, so as to preserve the focal spot size and the angle of incidence while shifting from one waveguide coupler to the other.

2.4. Nanoimaging of the field intensity

The nanoscale lateral resolution of the AFM-IR characterization technique is shown in Fig. 6. A $5 \times 5 \times 2$ μm^3 SU8 block was positioned at the output facet of an integrated Ge-on-Si waveguide under test. Radiation at $\lambda = 6.6$ μm, corresponding to both a strong MIR vibrational fingerprint
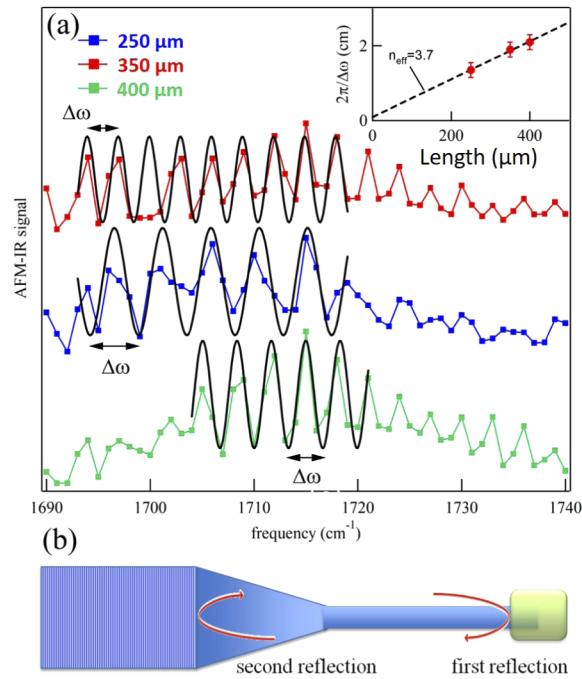
Fig. 5. (a) AFM-IR spectra showing Fabry-Perot cavity fringes for Ge-on-Si waveguide lengths of 250, 350, and 400 μm. Inset: linear fit to the measured fringe period as a function of cavity length. (b) A sketch of the cavity formed by the taper plus rectangular waveguide section.

of SU8 and a wavelength within the grating coupler spectrum fabricated at the input of the selected waveguide, was first sent directly to the SU8 block, and then coupled to the grating, similar to the experiment of Fig. 2. In Fig. 6(d), a SEM image of the block is shown: a ridge waveguide was employed for this specific experiment. The waveguide end buried below the SU8 appears as a dark rectangle in the AFM topography image in Fig. 6(a), highlighted with the same dashed contour also in Fig. 6(b)-(d).

The AFM-IR signal map of Fig. 6(b) was then acquired with the laser beam directly illuminating the block. Finally, the map of Fig. 6(c) was acquired with the laser beam sent to the grating (the MIR radiation then arrived to the SU8 block from the waveguide output facet). The direct illumination map in Fig. 6(b) shows that the whole block heats up due to the direct far-field illumination with a weaker temperature increase in the region corresponding to the buried waveguide. This is expected also due to the reduced thickness of the SU8 expansion layer on top of the waveguide (the expansion of Ge is negligible). The thermal conductance along the Ge waveguide also plays a role in decreasing the temperature of the SU8 layer portion in contact with it. Turning to Fig. 6(c) (waveguide illumination) one clearly sees that only the SU8 portion in front of the waveguide output facet is heated. The image represents, to a good approximation, the squared electric field intensity map outside the waveguide output facet. This is shown by thermal simulations where the previously calculated electromagnetic absorption is used as the heat source (Fig. 6(f), with Fig. 6(e) the corresponding reference simulation for direct illumination). From the analysis of the temperature maps, the nanoimaging resolution of our technique is evaluated in the 200-500 nm range, i.e. better than $\lambda/10$, limited by the 3D thermal diffusion lengths in the polymer block [39]. We point out that this information could not have been retrieved with any far-field technique because the near field at the output facet is non-propagating. In the simulations
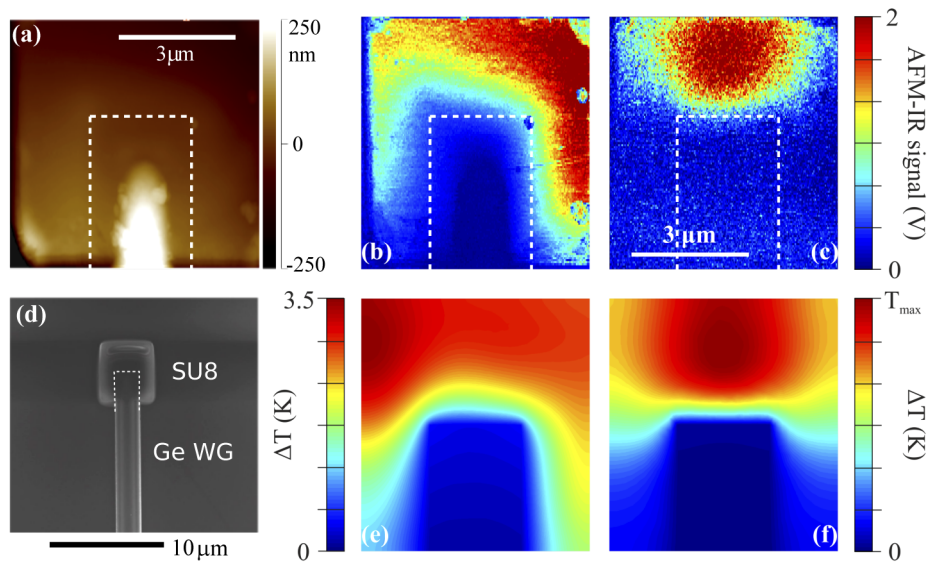
Fig. 6. The AFM-IR mapping of the field intensity at $\lambda = 6.6$ μm outside a waveguide output facet with sub-diffraction-limit resolution. (a) The AFM topography of the SU8 block partly covering the final portion of a ridge waveguide, indicated as dashed white contour in panels (a)-(d). (b) The AFM-IR signal map for direct illumination (input power of 8 mW). (c) The AFM-IR signal map for waveguide coupling (input power on the grating coupler of 100 mW). (d) A SEM image of the device on a larger scale. (e, f) Simulated temperature maps for the conditions (b, c) respectively, obtained with a combination of electromagnetic and thermal simulations.

of Fig. 6(f), single-mode propagation is assumed in the waveguide. The good comparison of the data of Fig. 6(c) with the numerical simulation of Fig. 6(f) confirms the excellent quality of the single-mode field pattern inside the fabricated waveguides, which ultimately defines the imaged near-field intensity pattern. The absolute value of the photo-induced temperature increase ΔT is obtained in the simulations of Fig. 6(e) by using the experimental input QCL power of ~ 8 mW (the QCL beam has been attenuated with mesh filters from its full power of 100 mW). In Fig. 6(f) the ΔT_{max} depends on the unknown grating coupler efficiency. The full QCL power of 100 mW was sent to the grating coupler, and the similar value of the maximum AFM-IR voltage signal ≈ 2 V in Fig. 6(b) and 6(c) suggests a similar value of the total MIR power reaching the block in the range of several mW, which would lead to grating coupler efficiencies below 10% (see Fig. 3(d)).

The numerical analysis was carried out by combining optical and thermal simulations. The optical simulations were performed using a full 3D FDTD method to extract the optical power density absorbed all over the SU8 volume both in the case of direct focused illumination and of single-mode illumination through the Ge waveguide. The results were then imported as heat sources in the thermal software, which employs a finite-element method to solve the heat diffusion equation (HEAT, Lumerical Inc., Canada). The steady-state temperature distribution inside the SU8 block was calculated, which is directly related to the measured AFM-IR signal. To set the proper boundary conditions in the thermal simulations, we impose a fixed temperature of 300 K at the bottom facet of the Si substrate, while keeping all the other free surfaces as thermal insulators. The thermal time constant obtained in the thermal simulations for our $5 \times 5 \times 2$ μm^3 blocks is 64 ns, and it could be reduced in future experiments by using smaller blocks at the expense of sensitivity. The analysis of Fig. 6 indicates that our technique may be suitable for

imaging more complex mode patterns in different kinds of mid-infrared waveguides, such as modes of different polarization or higher-order modes.

It is important to note the relatively short time required by the AFM-IR characterization measurements. The acquisition with our commercial AFM-IR system of a full spectrum from 900 to 1900 cm^{-1} like those of Fig. 4 takes less than 1 minute (integration time of 100 ms for 500 spectral points at 2 cm^{-1} frequency-scan step). At odds with our on-chip integrated photothermal detector, long integration times are usually required in far-field characterization techniques due to the low signal-to-noise ratio of MIR photodetectors. The acquisition of an AFM-IR map like those of Fig. 6(b) and 6(c) takes around 15 minutes (integration time of 100 ms for 10^4 pixels, pixel size $\approx 50 \times 50$ nm^2). Maps with sub-wavelength resolution cannot be acquired with far-field techniques. Automated serial testing of several waveguides on the same chip could be achieved by programming the AFM probe movement across the chip surface, which can be achieved because an extremely high (nanometric) positioning precision is not required. Polymers different from SU8 could be used, as long as they can be patterned by lithography and their etching recipes do not damage the waveguide structure (e.g. PMMA, AZ resins, HSQ,...). Finally, the photo-expanding polymer could be located anywhere on-chip, for example on top of the waveguide surface, provided that the evanescent field outside the Ge waveguide body is sufficiently strong to produce a high local temperature increase, but not so strong to disrupt the chip operation. The geometry would allow non-invasive testing of complex waveguide circuits. In summary, our technique could definitely help to speed up the development of MIR integrated circuits through the ability to measure the electric field profile and optical losses at discrete test points in the chips.

3. Conclusion

We have developed a novel technique for testing the operational performance of mid-infrared photonic integrated circuits using a nanoimaging and nanospectroscopy technique based on a wavelength-tunable MIR laser and an atomic force microscope. The IR intensity is mapped on the chip through the mechanical detection of the local photothermal expansion of polymer blocks patterned by lithography at specific test locations on the chip surface, effectively operating as integrated detectors. The experimental setup is based on a commercial AFM-IR instrument that was modified so as to physically decouple the AFM probe tip position from the laser illumination position. In this way, the MIR radiation from the laser is coupled at one end of the waveguide under test and the AFM probe detector is positioned at the other end. Three different tests were performed: i) nanoimaging of the near-field intensity at a waveguide output facet with lateral resolution better than $\lambda/10$ not limited by diffraction; ii) the spectral characterization of on-chip integrated Bragg grating couplers; iii) an estimate of propagation losses based on the observation of coherence effects in Fabry-Perot cavities. This list of tests is not exhaustive, as the characterization of many other physical quantities and waveguide configurations could be devised to assess waveguide performance parameters on-chip with sub-λ lateral resolution. The novel technique was here applied to ridge and rib waveguide chips made of heteroepitaxial Ge films grown on Si substrates. The material platform is here shown to operate in the wavelength range between 6 and 10 μm or broader, due to the high transparency of Ge in the MIR. Residual propagation losses of 3 dB/cm were measured at $\lambda = 6$ μm. In general, the presented technique is suitable for testing any MIR PIC platform, contributing to the development of integrated sensing schemes based on substance identification by unattended MIR vibrational fingerprint detection.

Acknowledgements

Disclosures

The authors declare no conflicts of interest.

References

1. M. Muneeb, X. Chen, P. Verheyen, G. Lepage, S. Pathak, E. Ryckeboer, A. Malik, B. Kuyken, M. Nedeljkovic, J. Van Campenhout, G. Z. Mashanovich, and G. Roelkens, "Demonstration of silicon-on-insulator mid-infrared spectrometers operating at 3.8 μm," Opt. Express **21**(10), 11659–11669 (2013).
2. P. T. Lin, S. W. Kwok, H.-Y. G. Lin, V. Singh, L. C. Kimerling, G. M. Whitesides, and A. Agarwal, "Mid-infrared spectrometer using opto-nanofluidic slot-waveguide for label-free on-chip chemical sensing," Nano Lett. **14**(1), 231–238 (2014).
3. L. C. Pacheco-Londono, W. Ortiz-Rivera, O. M. Primera-Pedrozo, and S. P. Hernandez-Rivera, "Vibrational spectroscopy standoff detection of explosives," Anal. Bioanal. Chem. **395**(2), 323–335 (2009).
4. M. Sieger, F. Balluff, X. Wang, S.-S. Kirn, L. Leidner, G. Gauglitz, and B. Mizaikof, "On-chip integrated mid-infrared GaAs/AlGaAs Mach-Zehnder interferometer," Anal. Chem. **85**(6), 3050–3052 (2013).
5. K. V. Oliver, A. Vilasi, A. Marechal, S. H. Moochhala, R. J. Unwin, and P. R. Rich, "Infrared vibrational spectroscopy: a rapid and novel diagnostic and monitoring tool for cystinuria," Sci. Rep. **6**(1), 34737 (2016).
6. M. R. Alcaráz, A. Schwaighofer, C. Kristament, G. Ramer, M. Brandstetter, H. Goicoechea, and B. Lendl, "External-cavity quantum cascade laser spectroscopy for mid-IR transmission measurements of proteins in aqueous solution," Anal. Chem. **87**(13), 6980–6987 (2015).
7. R. V. Rossel, D. Walvoort, A. McBratney, L. Janik, and J. Skjemstad, "Visible, near infrared, mid infrared or combined diffuse reflectance spectroscopy for simultaneous assessment of various soil properties," Geoderma **131**(1-2), 59–75 (2006).
8. J. Hodgkinson and R. P. Tatam, "Optical gas sensing: a review," Meas. Sci. Technol. **24**(1), 012004 (2013).
9. J. M. Hollas, *Modern spectroscopy* (J. Wiley, Chichester, Hoboken, NJ, 2004), 4th ed.
10. Y. Yu, X. Gai, T. Wang, P. Ma, R. P. Wang, Z. Y. Yang, D. Y. Choi, S. Madden, and B. Luther-Davies, "Mid-infrared supercontinuum generation in chalcogenides," Opt. Mater. Express **3**(8), 1075–1086 (2013).
11. X. Wang, J. Antoszewski, G. Putrino, W. Lei, L. Faraone, and B. Mizaikoff, "Mercury-cadmium-telluride waveguides - a novel strategy for on-chip mid-infrared sensors," Anal. Chem. **85**(22), 10648–10652 (2013).
12. S. Jung, D. Palaferri, K. Zhang, F. Xie, Y. Okuno, C. Pinzone, K. Lascola, and M. A. Belkin, "Homogeneous photonic integration of mid-infrared quantum cascade lasers with low-loss passive waveguides on an InP platform," Optica **6**(8), 1023–1030 (2019).
13. M. Brun, P. Labeye, G. Grand, J.-M. Hartmann, F. Boulila, M. Carras, and S. Nicoletti, "Low loss SiGe graded index waveguides for mid-IR applications," Opt. Express **22**(1), 508–518 (2014).
14. J. M. Ramirez, Q. Liu, V. Vakarin, J. Frigerio, A. Ballabio, X. L. Roux, D. Bouville, L. Vivien, G. Isella, and D. Marris-Morini, "Graded SiGe waveguides with broadband low-loss propagation in the mid infrared," Opt. Express **26**(2), 870–877 (2018).
15. Y.-C. Chang, V. Paeder, L. Hvozdara, J.-M. Hartmann, and H. P. Herzig, "Low-loss germanium strip waveguides on silicon for the mid-infrared," Opt. Lett. **37**(14), 2883–2885 (2012).
16. M. Nedeljkovic, J. S. Penades, V. Mittal, G. S. Murugan, A. Z. Khokhar, C. Littlejohns, L. G. Carpenter, C. B. E. Gawith, J. S. Wilkinson, and G. Z. Mashanovich, "Germanium-on-silicon waveguides operating at mid-infrared wavelengths up to 8.5 μm," Opt. Express **25**(22), 27431–27441 (2017).
17. K. Gallacher, R. W. Millar, U. Griskeviciute, L. Baldassarre, M. Sorel, M. Ortolani, and D. J. Paul, "Low loss Ge-on-Si waveguides operating in the 8-14 μm atmospheric transmission window," Opt. Express **26**(20), 25667–25675 (2018).
18. R. Soref, "Mid-infrared photonics in silicon and germanium," Nat. Photonics **4**(8), 495–497 (2010).
19. A. Malik, A. Spott, E. J. Stanton, J. D. Peters, J. D. Kirch, L. J. Mawste, D. Botez, J. R. Meyer, and J. E. Bowers, "Integration of mid-infrared light sources on silicon-based waveguide platforms in 3.5-4.7 μm wavelength range," IEEE J. Sel. Top. Quantum Electron. **25**(6), 1–9 (2019).
20. M. Sinobad, C. Monat, B. Luther-Davies, P. Ma, S. Madden, D. J. Moss, A. Mitchell, D. Allioux, R. Orobtchouk, S. Boutami, J. M. Hartmann, J. M. Fedeli, and C. Grillet, "Mid-infrared octave spanning supercontinuum generation to 8.5 μm in silicon-germanium waveguides," Optica **5**(4), 360–366 (2018).
21. M. P. Fischer, A. Riede, K. Gallacher, J. Frigerio, G. Pellegrini, M. Ortolani, D. J. Paul, G. Isella, A. Leitenstorfer, P. Biagioni, and D. Brida, "Plasmonic mid-infrared third harmonic generation in germanium nanoantennas," Light: Sci. Appl. **7**(1), 106 (2018).
22. K. Gallacher, A. Ballabio, R. W. Millar, J. Frigerio, A. Bashir, I. MacLaren, G. Isella, M. Ortolani, and D. J. Paul, "Mid-infrared intersubband absorption from p-Ge quantum wells grown on Si substrates," Appl. Phys. Lett. **108**(9), 091114 (2016).

23. Y. B. Wu, Z. B. Qu, A. Osman, W. Cao, A. Z. Khokhar, J. S. Penades, O. L. Muskens, G. Z. Mashanovich, and M. Nedelikovic, "Mid-infrared nanometallic antenna assisted silicon waveguide based bolometers," ACS Photonics **6**(12), 3253–3260 (2019).

24. Y. C. Chang, P. Waegli, V. Paeder, A. Homsy, L. Hvozdara, P. van der Wal, J. Di Francesco, N. F. de Rooij, and H. P. Herzig, "Cocaine detection by a mid-infrared waveguide integrated with a microfluidic chip," Lab Chip **12**(17), 3020–3023 (2012).

25. V. Mittal, M. Nedeljkovic, L. G. Carpenter, A. Z. Khokhar, H. M. H. Chong, G. Z. Mashanovich, P. N. Bartlett, and J. S. Wilkinson, "Waveguide absorption spectroscopy of bovine serum albumin in the mid-infrared fingerprint region," ACS Sens. **4**(7), 1749–1753 (2019).

26. U. Griškevičiūtė, R. W. Millar, K. Gallacher, J. Valente, and D. J. Paul, "Ge-on-Si waveguides for sensing in the molecular fingerprint regime," Opt. Express **28**(4), 5749–5757 (2020).

27. L. Baldassarre, E. Sakat, J. Frigerio, A. Samarelli, K. Gallacher, E. Calandrini, G. Isella, D. J. Paul, M. Ortolani, and P. Biagioni, "Midinfrared plasmon-enhanced spectroscopy with germanium antennas on silicon substrates," Nano Lett. **15**(11), 7225–7231 (2015).

28. J. Frigerio, A. Ballabio, K. Gallacher, V. Gilberti, L. Baldassarre, R. W. Millar, R. Milazzo, L. Maiolo, A. Minotti, F. Bottegoni, P. Biagioni, D. J. Paul, M. Ortolani, A. Pecora, E. Napolitani, and G. Isella, "Optical properties of highly n-doped germanium obtained by in situ doping and laser annealing," J. Phys. D: Appl. Phys. **50**(46), 465103 (2017).

29. K. Gallacher, R. W. Millar, U. Griškevičiūtė, M. Sinclair, M. Sorel, L. Baldassarre, M. Ortolani, R. Soref, and D. J. Paul, "Ultra-broadband mid-infrared Ge-on-Si waveguide polarization rotator," APL Photonics **5**(2), 026102 (2020).

30. S. Radosavljevic, N. T. Beneitez, A. Katumba, M. Muneeb, M. Vanslembrouck, B. Kuyken, and G. Roelkens, "Mid-infrared vernier racetrack resonator tunable filter implemented on a germanium on SOI waveguide platform invited," Opt. Mater. Express **8**(4), 824–835 (2018).

31. A. Malik, M. Muneeb, S. Pathak, Y. Shimura, J. Van Campenhout, R. Loo, and G. Roelkens, "Germanium-on-silicon mid-infrared arrayed waveguide grating multiplexers," IEEE Photonics Technol. Lett. **25**(18), 1805–1808 (2013).

32. C. Alonso-Ramos, M. Nedeljkovic, D. Benedikovic, J. S. Penades, C. G. Littlejohns, A. Z. Khokhar, D. Perez-Galacho, L. Vivien, P. Cheben, and G. Z. Mashanovich, "Germanium-on-silicon mid-infrared grating couplers with low-reflectivity inverse taper excitation," Opt. Lett. **41**(18), 4324–4327 (2016).

33. M. Nedeljkovic, A. V. Velasco, A. Z. Khokhar, A. Delage, P. Cheben, and G. Z. Mashanovich, "Mid-infrared silicon-on-insulator Fourier-transform spectrometer chip," IEEE Photonics Technol. Lett. **28**(4), 528–531 (2016).

34. M. Montesinos-Ballester, Q. K. Liu, V. Vakarin, J. M. Ramirez, C. Alonso-Ramos, X. Le Roux, J. Frigerio, A. Ballabio, E. Talamas, L. Vivien, G. Isella, and D. Marris-Morini, "On-chip Fourier-transform spectrometer based on spatial heterodyning tuned by thermo-optic effect," Sci. Rep. **9**(1), 14633 (2019).

35. A. Apuzzo, M. Février, R. Salas-Montiel, A. Bruyant, A. Chelnokov, G. Lérondel, B. Dagens, and S. Blaize, "Observation of near-field dipolar interactions involved in a metal nanoparticle chain waveguide," Nano Lett. **13**(3), 1000–1006 (2013).

36. P. Sarriugarte, M. Schnell, A. Chuvilin, and R. Hillenbrand, "Polarization-resolved near-field characterization of nanoscale infrared modes in transmission lines fabricated by gallium and helium ion beam milling," ACS Photonics **1**(7), 604–611 (2014).

37. F. La China, F. Intonti, N. Caselli, F. Lotti, F. Sarti, A. Vinattieri, A. Noury, X. Le Roux, W. Zhang, E. Cassan, C. A. Ramos, E. D. Valdeiglesias, N. Izard, L. Vivien, and M. Gurioli, "Near-field Fano-imaging of TE and TM modes in silicon microrings," ACS Photonics **2**(12), 1712–1718 (2015).

38. B. J. M. Brenny, D. M. Beggs, R. E. C. van der Wel, L. Kuipers, and A. Polman, "Near-infrared spectroscopic cathodoluminescence imaging polarimetry on silicon photonic crystal waveguides," ACS Photonics **3**(11), 2112–2121 (2016).

39. A. Dazzi and C. B. Prater, "AFM-IR: Technology and applications in nanoscale infrared spectroscopy and chemical imaging," Chem. Rev. **117**(7), 5146–5173 (2017).

40. F. Lu, M. Jin, and M. A. Belkin, "Tip-enhanced infrared nanospectroscopy via molecular expansion force detection," Nat. Photonics **8**(4), 307–312 (2014).

41. V. Giliberti, R. Polito, E. Ritter, M. Broser, P. Hegemann, L. Puskar, U. Schade, L. Zanetti-Polzi, I. Daidone, S. Corni, F. Rusconi, P. Biagioni, L. Baldassarre, and M. Ortolani, "Tip-enhanced infrared difference-nanospectroscopy of the proton pump activity of bacteriorhodopsin in single purple membrane patches," Nano Lett. **19**(5), 3104–3114 (2019).

42. B. Lahiri, G. Holland, V. Aksyuk, and A. Centrone, "Nanoscale imaging of plasmonic hot spots and dark modes with the photothermal-induced resonance technique," Nano Lett. **13**(7), 3218–3224 (2013).

43. A. Centrone, "Infrared imaging and spectroscopy beyond the diffraction limit," Annu. Rev. Anal. Chem. **8**(1), 101–126 (2015).

44. E. Calandrini, T. Venanzi, F. Appugliese, M. Badioli, V. Giliberti, L. Baldassarre, P. Biagioni, F. De Angelis, W. M. Klesse, G. Scappucci, and M. Ortolani, "Mapping the electromagnetic field confinement in the gap of germanium nanoantennas with plasma wavelength of 4.5 micrometers," Appl. Phys. Lett. **109**(12), 121104 (2016).

45. A. Mancini, V. Giliberti, A. Alabastri, E. Calandrini, F. De Angelis, D. Garoli, and M. Ortolani, "Thermoplasmonic effect of surface-enhanced infrared absorption in vertical nanoantenna arrays," J. Phys. Chem. C **122**(24), 13072–13081 (2018).

46. J. R. Felts, K. Kjoller, M. Lo, C. B. Prater, and W. P. King, "Nanometer-scale infrared spectroscopy of heterogeneous polymer nanostructures fabricated by tip-based nanofabrication," ACS Nano **6**(9), 8015–8021 (2012).

47. L. Baldassarre, V. Giliberti, A. Rosa, M. Ortolani, A. Bonamore, P. Baiocco, K. Kjoller, P. Calvani, and A. Nucara, "Mapping the amide-I absorption in single bacteria and mammalian cells with resonant infrared nanospectroscopy," Nanotechnology **27**(7), 075101 (2016).

48. V. Giliberti, M. Badioli, A. Nucara, P. Calvani, E. Ritter, L. Puskar, E. F. Aziz, P. Hegemann, U. Schade, M. Ortolani, and L. Baldassarre, "Heterogeneity of the transmembrane protein conformation in purple membranes identified by infrared nanospectroscopy," Small **13**(44), 1701181 (2017).

49. B. T. O'Callahan, J. Yan, F. Menges, E. A. Muller, and M. B. Raschke, "Photoinduced tip-sample forces for chemical nanoimaging and spectroscopy," Nano Lett. **18**(9), 5499–5505 (2018).

50. J. Chae, S. An, G. Ramer, V. Stavila, G. Holland, Y. Yoon, A. A. Talin, M. Allendorf, V. A. Aksyuk, and A. Centrone, "Nanophotonic atomic force microscope transducers enable chemical composition and thermal conductivity measurements at the nanoscale," Nano Lett. **17**(9), 5587–5594 (2017).

51. G. Ramer, V. A. Aksyuk, and A. Centrone, "Quantitative chemical analysis at the nanoscale using the photothermal induced resonance technique," Anal. Chem. **89**(24), 13524–13531 (2017).

52. S. Cecchi, E. Gatti, D. Chrastina, J. Frigerio, E. Müller Gubler, D. J. Paul, M. Guzzi, and G. Isella, "Thin SiGe virtual substrates for Ge heterostructures integration on silicon," J. Appl. Phys. **115**(9), 093502 (2014).

53. Y. Zhang, S. Y. Yang, A. E. J. Lim, G. Q. Lo, C. Galland, T. Baehr-Jones, and M. Hochberg, "A compact and low loss Y-junction for submicron silicon waveguide," Opt. Express **21**(1), 1310–1316 (2013).

54. C. Florea and K. A. Winick, "Fabrication and characterization of photonic devices directly written in glass using femtosecond laser pulses," J. Lightwave Technol. **21**(1), 246–253 (2003).